JGR Space Physics

RESEARCH ARTICLE
10.1029/2022JA030261

Comparing and Contrasting the Properties of the Inner Heliosphere for the Three Most Recent Solar Minima

Pete Riley[1], Ronald M. Caplan[1], Cooper Downs[1], Jon A. Linker[1], and Roberto Lionello[1]

[1]Predictive Science Inc, San Diego, CA, USA

Key Points:

- Solar indices suggest that the two last minima (2008 and 2019) represent a notable decrease in levels of activity
- Solar wind measurements suggest that the most recent minimum was a partial recovery from the 2008 minimum
- MHD model results provide a global context for interpreting the solar and in-situ measurements

Correspondence to:
P. Riley,
pete@predsci.com

Citation:
Riley, P., Caplan, R. M., Downs, C., Linker, J. A., & Lionello, R. (2022). Comparing and contrasting the properties of the inner heliosphere for the three most recent solar minima. *Journal of Geophysical Research: Space Physics*, *127*, e2022JA030261. https://doi.org/10.1029/2022JA030261

Received 7 JAN 2022
Accepted 27 JUL 2022

Abstract The previous three solar cycles have ended in progressively more quiescent conditions, suggesting a continual slide into an ever deeper minimum state. Although the Sun's magnetic field is undoubtedly responsible for this quiescence, it is not clear how changes in its structure and strength modulate the properties of the solar wind. In this study, we compare the statistical properties of the solar wind during the three most recent minima (08/1996, 12/2008, and 12/2019) and develop global MHD model solutions to help interpret these observations. We find that, counter-intuitively, the statistical properties of the solar wind for the most recent minimum lie midway between the 08/1996 and 12/2008 minima. For example, while the minimum speed dropped by 40 km s^{-1} between 08/1996 and 12/2008, they rose by 20 km s^{-1} around the 12/2019 minimum. From the model results, we infer that the 12/2008 and 12/2019 minima were structurally similar to one another, with the presence of corotating interaction regions driven by equatorial coronal holes, while the 08/1996 minimum represented a more "standard" tilted dipole configuration associated with those of earlier space age minima. Comparison of the statistical properties derived from the model results with data suggest several opportunities to improve model parameters, as well as to apply more sophisticated modeling approaches. Overall, however, the model results capture the essential features of the observations and, thus, allow us to infer the global structure of the inner heliosphere, of which the *in-situ* measurements provide only a glimpse.

1. Introduction

Solar minimum is the point in the solar activity cycle corresponding to a local minimum in sunspot activity. Typically, although not universally accepted, solar minimum is identified by inspecting a smoothed 12-month running average of sunspot data; thus, the minimum cannot be officially recognized until at least 6 months following its actual occurrence (Harvey & White, 1999). Solar cycles 22, 23 and 24 ended with a solar minimum in 08/1996 (e.g., de Toma et al., 2000), 12/2008 (e.g., Solomon et al., 2010), and 12/2019 (e.g., Finsterle et al., 2021), respectively. In addition to regular 11-year cycles, a number of longer, or grand solar minima and maxima have been identified (e.g., Eddy, 1976). For example, the Maunder Minimum is defined as the interval between 1645 and 1715 (e.g., Riley, Lionello, et al., 2015). More recently, the so-called "modern maximum" has been defined as from 1914 through 2008. From 2008 through the present, solar activity has been substantially less than during the previous epoch defined by the space era. Whether this trend continues into the future, resulting in a grand minimum being defined (with the proposed name of the "Eddy Minimum" (e.g., Riley, 2018)), remains to be seen.

During the late declining phase of the solar cycle and at solar minimum, as the number of active regions decreases, the structure of the solar corona, and by extension, the heliosphere, is governed by the largest components of the magnetic field, and, the dipole component, in particular. This leads to a predictable pattern of corotating interaction regions and rarefactions in the solar wind that persists from one rotation to the next. Of particular note, the radial velocity of the solar wind is the primary driver of dynamic evolution (e.g., Riley et al., 2003). In the declining phase, for example, we can picture a band of slow solar wind, entraining the heliospheric current sheet (HCS), and organized about the heliomagnetic equator, which is tilted with respect to the rotation axis. As the Sun rotates, faster solar wind is placed underneath previously-released, slower wind, catching it and compressing it, and resulting in a compression region. In contrast, where faster solar wind outruns slower wind behind, a rarefaction region (or expansion wave) is created. These processes lead to a remarkably predictable pattern in the location and orientation of corotating interaction regions (CIRs) in the heliosphere, including the forward and reverse shocks that bound them beyond 1 AU. Prior to the 2008 minimum, this was the general picture inferred from the available observations (e.g., Riley et al., 2001). However, data obtained during the approach to the 2008 minimum suggested that this picture must be generalized to include the effects of equatorial coronal holes (e.g., Riley et al., 2011). Such holes were typically more a feature of higher solar activity; however, due primarily to the much

weaker polar fields, equatorial coronal holes were able to develop, in concert with associated pseudo-streamers (e.g., Riley et al., 2011). Equatorial coronal holes also produce a predictable structure in the solar wind: In this case, slow wind to the west of an equatorial coronal hole is caught and compressed by the fast wind. To the east, the slow flow is outrun by the fast wind generating an expansion wave. Given the roughly circular shape of the equatorial holes, the structures that result are often sideways "U" or "V" shapes (Riley et al., 2011). Based on these intuitive visualisations, we can assemble a qualitative picture of how structure will develop and evolve in the inner heliosphere.

Global MHD models support these ideas. Pizzo and Gosling (1994) first provided an interpretation of the orientation of CIR-driven shocks observed by Ulysses observations using an idealized 3-D MHD model. Later, Riley et al. (2001); Riley et al. (2003) built on these ideas to provide a more comprehensive, global perspective to interpret the in situ measurements. This included the systematic tilting of CIRs with respect to latitude and heliocentric distance, as well as the relative position of the HCS with respect to CIRs. More recent analyses of the 2008 minimum emphasized the role played by pseudo-streamers in organizing solar wind structure (e.g., Riley et al., 2011; Riley, Linker, Americo Gonzalez Esparza et al., 2012; Riley & Luhmann, 2012).

A number of studies have already compared and contrasted the solar minima at the end of cycles 22 and 23 (e.g., Gibson et al., 2009). From a global perspective, studies analyzing Ulysses measurements are particularly relevant (e.g., McComas et al., 2006). Although Ulysses sampled the polar regions prior to the 23/24 minima (early 2008), the data provide an extended snapshot of the properties of the 3-D heliosphere during the late declining phase of the solar cycle, and, when combined with near-Earth measurements, could be used to reasonably extrapolate conditions at solar minimum (e.g., Riley et al., 2010). Several points are worth noting about these polar crossings. First, the solar wind speed did not appreciably change between 1994-1995 and 2007–2008 (McComas et al., 2008). On the other hand, the plasma number density decreased by approximately 17%, suggesting that the wind of the 23/24 cycle was less heated than during the prior minimum (McComas et al., 2008; Riley et al., 2010). Additionally, decreases in the measured radial magnetic field were correlated with decreases in plasma density (Ebert et al., 2009; Riley et al., 2010; Schwadron & McComas, 2008), and, moreover, these interplanetary field decreases were also well correlated with decreases in the photospheric magnetic field. Thus, the lower photospheric magnetic field strengths, and particularly the polar field strengths, together with the lower number densities, suggest a weaker source of slow solar wind. Moreover, while CIRs may not be as well developed in weaker cycles, given that the structures are less constrained by the weaker overlying dipole field, they may extend farther poleward.

The 2008 minimum (marking the end of cycle 23 and the beginning of cycle 24) was unique (at least on the time-scale of a century) in several key ways (Gibson et al., 2011). Riley, Lionello, et al. (2012) provided a detailed analysis of global MHD model results for the "Whole Heliosphere Interval" (WHI), which occurred from 20 March through 16 April 2008, or, shortly before the minimum. They compared white light and emission images, as well as *in-situ* measurements providing support that the large-scale 3-D structure suggested by the model was likely correct. Unlike previously modeled minima (e.g., Riley et al., 2001), they found that the orientation of CIRs and their associated shocks were not nearly as well ordered as previously. As noted earlier, these differences could be attributed to a reduced polar photospheric flux (~40%) (Svalgaard & Cliver, 2007, June), which resulted in polar coronal holes that were notably smaller (Kirk et al., 2009). This, in turn, allowed equatorial coronal holes to open up, resulting in the more complex CIR structure. An additional consequence of the smaller polar flux was the formation of pseudo-streamers in the corona, which were much less frequent during previous minima (Riley & Luhmann, 2012). Additionally, Riley, Linker, Americo Gonzalez Esparza, et al. (2012) analyzed the large-scale structure of the inner heliosphere surrounding the 23/24 minimum, and compared it with the previous minimum using a global MHD model. They focused on understanding the properties of CIRs observed during the two intervals, and, in particular, on the orientation of stream interfaces (SIs), which separate wind that was initially slow and dense, from wind that was originally fast and tenuous. They found that while the E–W (azimuthal) orientations of the CIRs were regular, and aligned with the nominal Parker spiral direction, N–W (meridional) deflections were much more irregular during the 23/24 minimum than the previous one (22/23 minimum), which showed a systematic pattern of alternating tilts (e.g., Riley et al. (1996, 2001)).

In this study, we compare the statistical properties of the solar wind, as inferred from Earth-Based spacecraft and Ulysses. We focus on the basic plasma and magnetic field parameters, including speed, density, magnetic field strength, as well as mass and momentum flux. We also relate the inferred variations to variations in solar

parameters, and, sunspot number (SSN) and polar field strengths, in particular. Then, we develop a set of global MHD model results corresponding to the minimum between cycles, 22/23, 23/24, and 24/25 in an effort to understand the similarities and differences in the observed data between these three epochs. In the next section, we describe the observations used to drive the model as well as the *in-situ* measurements used to validate the results. We also discuss the MHD approach used to develop the model solutions. In Section 3, we present our results, beginning with a detailed analysis of both solar and *in-situ* measurements for each of the solar minima, pointing out the similarities and differences, and leveraging the overlapping data of Ulysses and Earth-based spacecraft to infer global properties for the most recent minimum, for which Ulysses data were not available. Following this, we compare model results with *in-situ* measurements as a way of validating the model results, pointing out where the major disagreements lie. Then, we use the model results to infer the global structure of the heliosphere for each minimum, including the properties of CIRs and rarefaction regions, and the shape of the HCS. Finally, we summarize our main findings, discuss the limitations of the study, and suggest how future studies may shed further light on this topic.

2. Methods

2.1. Data

For this study, we use photospheric magnetic field observations from: (a) the Michelson Doppler Imager (MDI) onboard the Solar and Heliospheric Observatory (SOHO) spacecraft (Scherrer et al., 1995) for the 22/23 minimum; and (b) the Helioseismic and Magnetic Imager (HMI) onboard the Solar Dynamics Observatory (SDO) spacecraft (Scherrer et al., 2012) for the 23/24 and 24/25 minima. The data were obtained from the Joint Science Operations Center (JSOC, Scherrer et al., 2010). MDI/HMI data provide an estimate for the radial component of the field on a uniform grid size of 3,600 × 1,440 in longitude and sin(latitude), respectively. The processing of these data into boundary conditions suitable for driving the MHD model has been described in detail elsewhere (e.g., Caplan, Downs, & Linker, 2019; Riley et al., 2014).

We use *in-situ* measurements from ACE and Wind, in the form of the merged OMNI dataset as well as from Ulysses. The OMNI dataset is made up of hourly-averaged near-Earth solar wind magnetic field and plasma measurements from several geocentric of L1 orbits, depending on the particular epoch of the observations (e.g., Papitashvili et al., 2000). For the data analyzed here, Wind and ACE spacecraft provided the measurements (McComas et al., 1998; Ogilvie et al., 1995). The Ulysses spacecraft was launched in October 1990. After receiving a gravity assist from Jupiter in February 1992, it entered into a highly eccentric orbit, reaching maximum heliographic latitudes of ±80.2° during each of its three, roughly 5.5 years orbits (McComas et al., 2000). Each orbit consisted of a slow phase, during which it reached an aphelion of 5.4 AU and a so-called "rapid latitude scan" where perihelion occurred at 1.34 AU. The solar wind plasma experiment on board Ulysses, SWOOPS, consisted of two electrostatic analyzers measuring proton and electron distribution functions as a function of energy per charge and direction (McComas et al., 1998).

From each spacecraft we compare solar wind bulk speed, proton number density, and radial magnetic field. Together, these three quantities characterize the basic dynamical properties of the solar wind. All data were obtained from NASA's Space Physics Data Facility (SPDF) web services API (e.g., Candey et al., 2019), and were retrieved at 1-hr resolution. Additionally, using the plasma density (N_p) and bulk plasma velocity (v), we estimate the momentum flux ($N_p \times v \times r^2$) and mass flux ($n \times v \times r^2$) of the solar wind, where r is heliocentric distance and is used to scale density measurements to those measured at 1 AU. Momentum flux is reported in units of amu m^{-1} s^{-2}, while mass flux at 1 AU is given in units of amu-m^{-2} s^{-1}.

2.2. Models

In this study, we use the MAS (Magnetohydrodynamic Algorithm outside a Sphere) code, which solves the usual set of resistive MHD equations in spherical coordinates on a non-uniform mesh. The details of the model have been described elsewhere (e.g., Caplan, Linker, et al., 2019; Lionello et al., 2001; Mikić & Linker, 1994; Mikic et al., 2018; Mikić et al., 2018a; Riley et al., 2001; Riley, Lionello, et al., 2012). Here, we restrict our description to several relevant points. First, the model is driven by the observed photospheric magnetic field. We use MDI/HMI observations from the SOHO/SDO spacecraft to construct a boundary condition for the radial magnetic field at $1R_S$ as a function of latitude and longitude. Second, the model is run in two stages: the region from 1 to

$30R_S$ is first modeled, followed by the region from $30R_S$ to 1 AU, which is driven directly by the results of the coronal calculation. Computationally, this approach is much more efficient. Third, for these solutions, we use a single map to cover an entire solar rotation; thus, although the model is time-dependent, it is run forward in time until a dynamic steady-state is achieved. This is a reasonable approximation when structure at the Sun is not appreciably changing from one rotation to the next. Fourth, MAS relies on a variety of approximations to reconstruct (or predict) the large-scale structure and properties of the solar corona and inner heliosphere. In order of increasing complexity (and historical development), we refer to them as the 'polytropic', 'thermodynamic' and Wave-Turbulence-Driven ('WTD') models. For this study, we use the 'semi-empirical thermodynamic' solutions, which have been shown to consistently provide better solutions in terms of matching *in-situ* measurements at Earth, STEREO A and Parker Solar Probe (PSP) (Riley et al., 2020).

The thermodynamic approximation relies on an empirically-based treatment of energy transport processes (radiation losses, heat flux, and coronal heating) in the corona (Lionello et al., 2001; Lionello et al., 2009), and in this case, γ is set to $\frac{5}{3}$ (as opposed to 1.05 for the polytropic approximation). Development of this model focused on improving the density and temperature structure in the solar corona through comparisons with EUV and X-ray images from a variety of spacecraft. Relatively little direct comparison was performed with *in-situ* measurements, Thus, we implement the "Distance from the Coronal Hole Boundary" (DCHB) approximation (where the velocity profile is a function of the perpendicular distance from the nearest coronal hole boundary) to derive the heliospheric boundary conditions from the thermodynamic solution (Riley et al., 2001). In this sense, the model is not fully thermodynamic, and, hence, the label "semi-empirical thermodynamic" model. When we have produced complete end-to-end coronal-heliospheric thermodynamic solutions, we have found that they do not reproduce the observed structure in the solar wind at 1 AU as accurately as the "semi-empirical" approximation, even though they correctly match the observed amplitude of the quantities.

We ran model solutions at both "medium" resolution ($101 \times 101 \times 129$ for the corona and $141 \times 111 \times 128$ for the heliosphere) and "high" resolution ($255 \times 143 \times 300$ for the corona and $500 \times 157 \times 361$ for the heliosphere) to ensure that the size of the grid had no material effect on the results, which it did not. Here, we present the results from the high-resolution solutions.

3. Results

3.1. Analysis of the Data

In this Section, we present our results, starting with an analysis of both remote solar observations and *in-situ* plasma and magnetic field measurements for each of the solar minima. We emphasize the large-scale similarities and differences, and leverage the overlapping data of Ulysses and Earth-based spacecraft to infer the likely global properties for the most recent minimum, for which Ulysses data were not available. We also consider the statistical properties of the in-ecliptic measurements in both the time and spectral domains.

We begin by briefly reviewing some of the global properties of the Sun for each of the last three solar minima. First, in Figure 1a we present the daily (red) and monthly running average (blue) sunspot numbers from the Sunspot Index and Long-term Solar Observations (SILSO) dataset, which includes a careful re-calibration of the dataset (Clette & Lefèvre, 2016). This is a useful parameter in the sense that it captures, at least indirectly, a measure of the complexity of the photospheric magnetic field, and, in particular, the number of active regions currently visible on the solar disk. Several features are apparent. First, the amplitude of successive maxima decreases from cycles 23–25. Second, there is evidence for a bi-modal peak in the time series for each of the maxima. Third, the depth and duration of the troughs at solar minimum also increase, with evidence that the sunspot number "bottoms out" at the beginning of cycles 24 and 25. To better investigate the differences between the cycles, in Figure 1b we have aligned each solar minimum with a time of zero, and plotted the evolution of the profile over the course of 12 years. Thus, each curve captures the second half of one cycle and the first half of the next. Here, we can see the differences in profiles more clearly, with interval 22–23 showing the strongest gradient both in the decay and rise of SSN. Intervals 23–24 (green) and 24–25 (blue), on the other hand are both more gradual, and more similar to one another. Thus, based on this, we anticipate that the climb out from the solar minimum of 12/2019 will continue to be more shallow than 22–23, and, much more similar to that of 23–24. In so far as SSN acts as a proxy for solar activity, this figure also emphasizes the increase in duration of solar-minimum-like

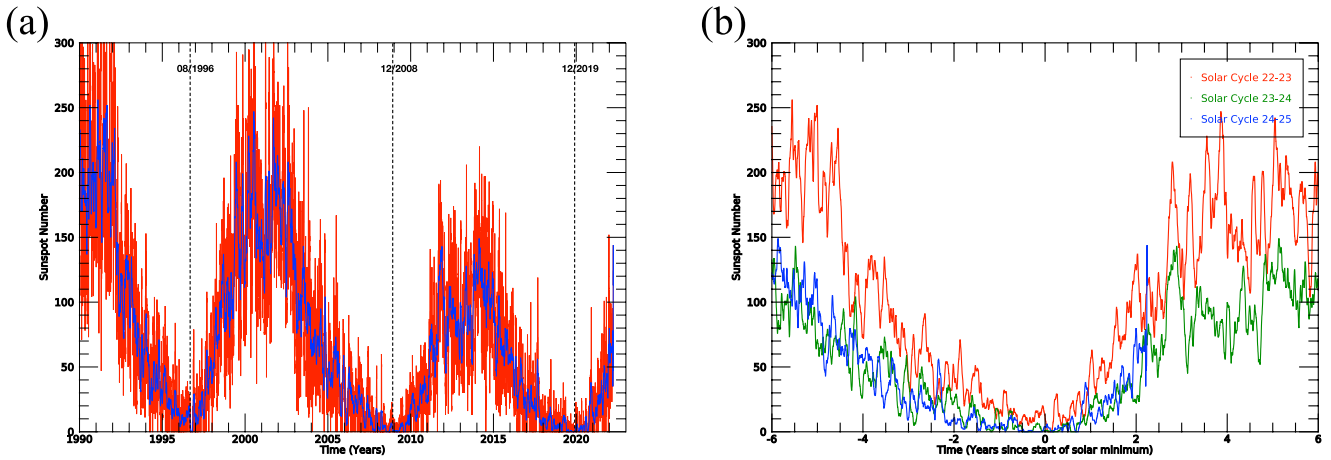

Figure 1. (a) Daily (red) and monthly running average (blue) sunspot number as a function of time covering the last three solar minima (08/1996, 12/2008, and 12/2019). (b) As (a) but with time synchronized with solar minimum at the end of cycles 22 (red), 23 (green), and 24 (blue).

conditions. If we arbitrarily define "solar minimum conditions" to be where $SSN < 20$, say, then the 22–23 minimum lasted ∼1.5 years, whereas the 23–24 and 24–25 minima lasted ∼3 years.

A second useful parameter to consider is the solar polar field strength, as inferred from photospheric observations. This complements sunspot number in the sense that it is a measure of the largest-scale magnetic fields visible on the Sun. For this, we use values estimated from the Wilcox solar observatory (e.g., Hoeksema, 1992). It is constructed by using the poleward most 3' apertures (corresponding to line-of-sight fields between 55° and the pole) each day, for both the north and south. The data are averaged over 10 days and a 20-nhz low-pass filter has been applied to reduce yearly geometrical projection effects. Figure 2 (a) summarizes the data from the northern polar regions (red), southern polar regions (blue) and signed average (black) as a function of time from 1990 through early 2022. We note several points. First, there is a clear yearly oscillation in the northern and southern profiles due to the relative tilt of the Earth with respect to the Sun's equatorial plane (Hoeksema et al., 1983). This is generally removed when the two are averaged (black curve). Second, the northern and southern polar regions are relatively symmetric in their overall amplitude and modulation during this time period. Third, the fields peak and plateau 5 years or so prior to each solar minimum, holding steady for several years, then beginning their decline prior to solar minimum, and continuing toward zero, which they reach at solar maximum. Indirectly, this profile illustrates the relative contribution to the Sun's magnetic field played from the axial dipole component,

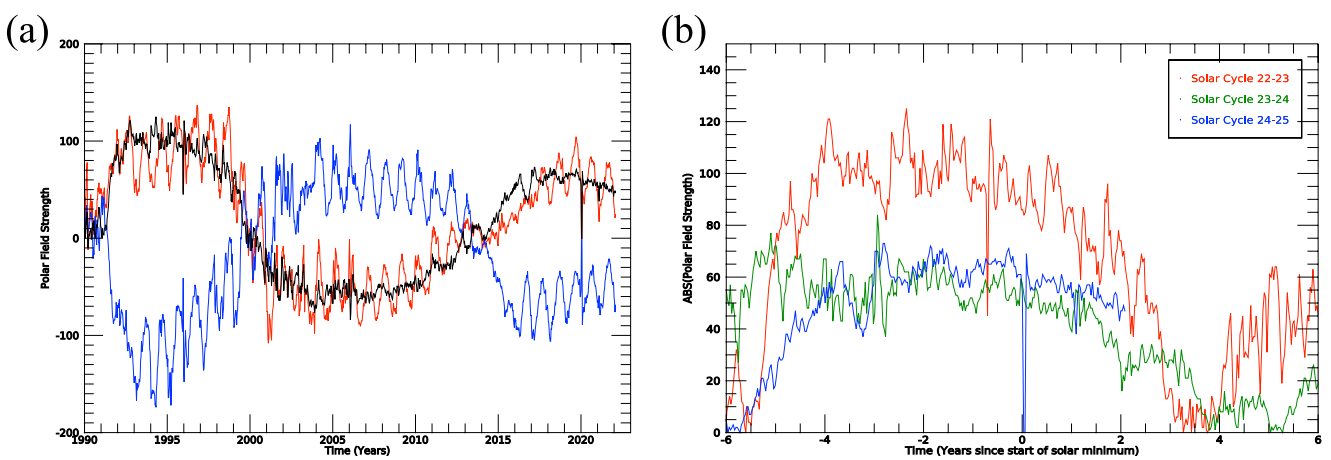

Figure 2. (a) Wilcox Solar Observatory polar magnetic field observations as a function of time. The curves represent the northern polar regions (red), southern polar regions (blue), and signed average (black). (b) The average, unsigned polar magnetic field strength (black curve from (a)) but with time synchronized with solar minimum at the end of cycles 22 (red), 23 (green), and 24 (blue).

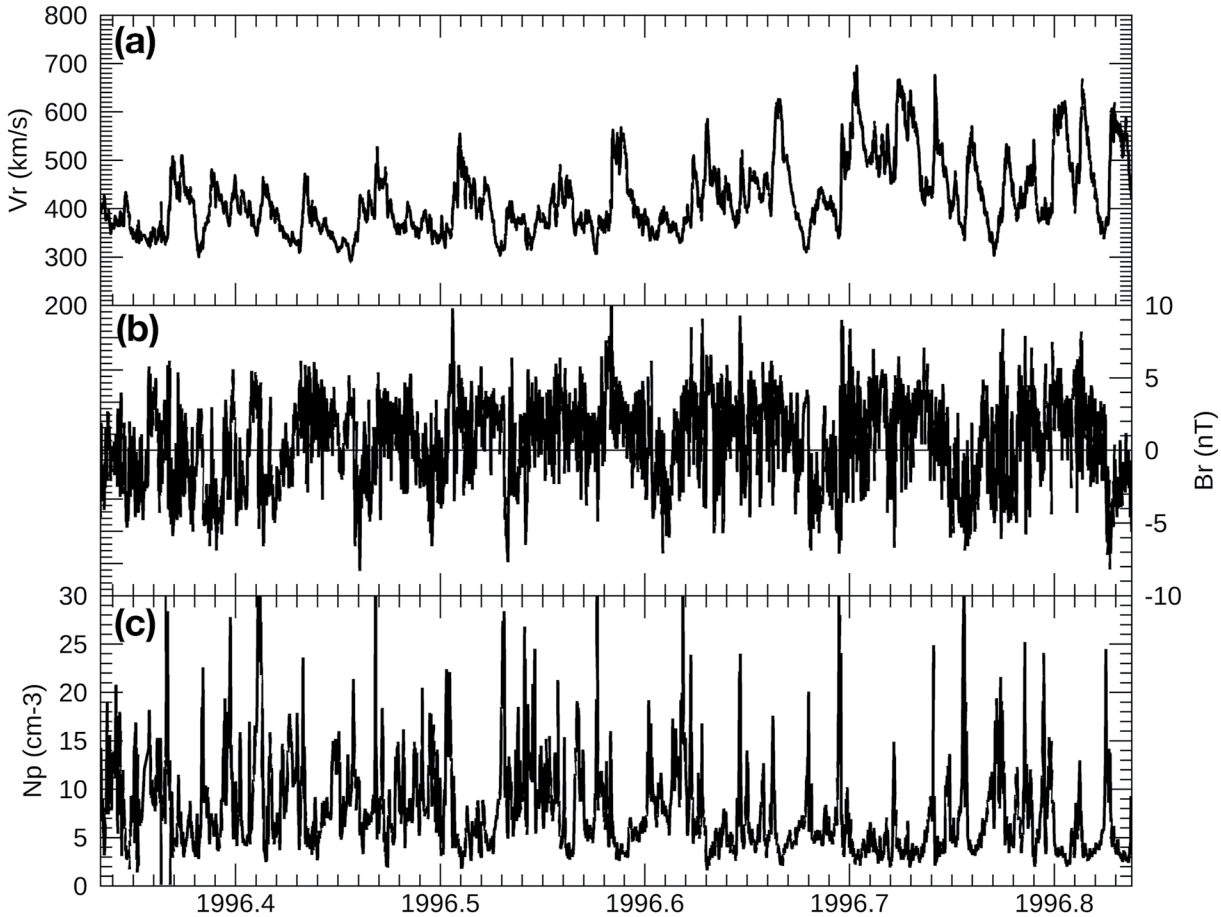

Figure 3. Time series of (a) solar wind speed (v_r), (b) radial magnetic field (B_r), and (c) plasma number density (N_p) as a function of time for 3 months prior to, and following the solar minimum of 08/1996.

as oppose to higher-order moments; the latter of which play an ever increasing role as solar activity increases (Hoeksema et al., 1983).

Again, to better compare the fields surrounding each of the last three solar minima, we can overlay the average polar field strengths, aligning them with the minimum in the solar activity cycle (Figure 2b). For a clearer comparison, we show the absolute magnitude of the average polar field. Solar minima in these plots arrives at year zero. Unsurprisingly, the minimum defined by the start of cycle 23 is associated with the largest polar fields, which are (~67%) larger than those observed in the following minima (green and blue). The only notable difference between the latter two is that the overall amplitude is slightly (~15%) higher for cycle 25.

Moving into the solar wind, in Figure 3, we summarize *in-situ* measurements from the OMNI dataset at 1 AU: (a) solar wind speed (v_r), (b) radial magnetic field (B_r), and (c) plasma number density (N_p) as a function of time from 05/1996 through 11/1996, or, an interval of 6 months surrounding solar minimum. We note several points. First, a clear periodicity on the timescale of the solar rotation can be seen in the data, particularly in solar wind velocity, with modest, recurrent (500 km s^{-1}) streams occurring prior to, and following the minimum. After the minimum, the size of the streams increases, approaching 700 km s^{-1}. Second, and although less apparent, this recurrent pattern is also visible as sector crossings in the radial magnetic field, which alternates between ±5 nT throughout the interval. Third, the compression regions created by these streams (where the peak densities align with the speed gradients marking the boundaries between slow and fast wind) are visible in peak densities often exceeding 25 cm^{-3} during this interval. Fourth, the base density during this period is consistently ~3 cm^{-3}.

Figure 4 presents the same information for the 23/24 minimum. While many of the same points can be made, there are some notable differences. For example, the high-speed streams prior to the minimum are larger (~700 km s^{-1})

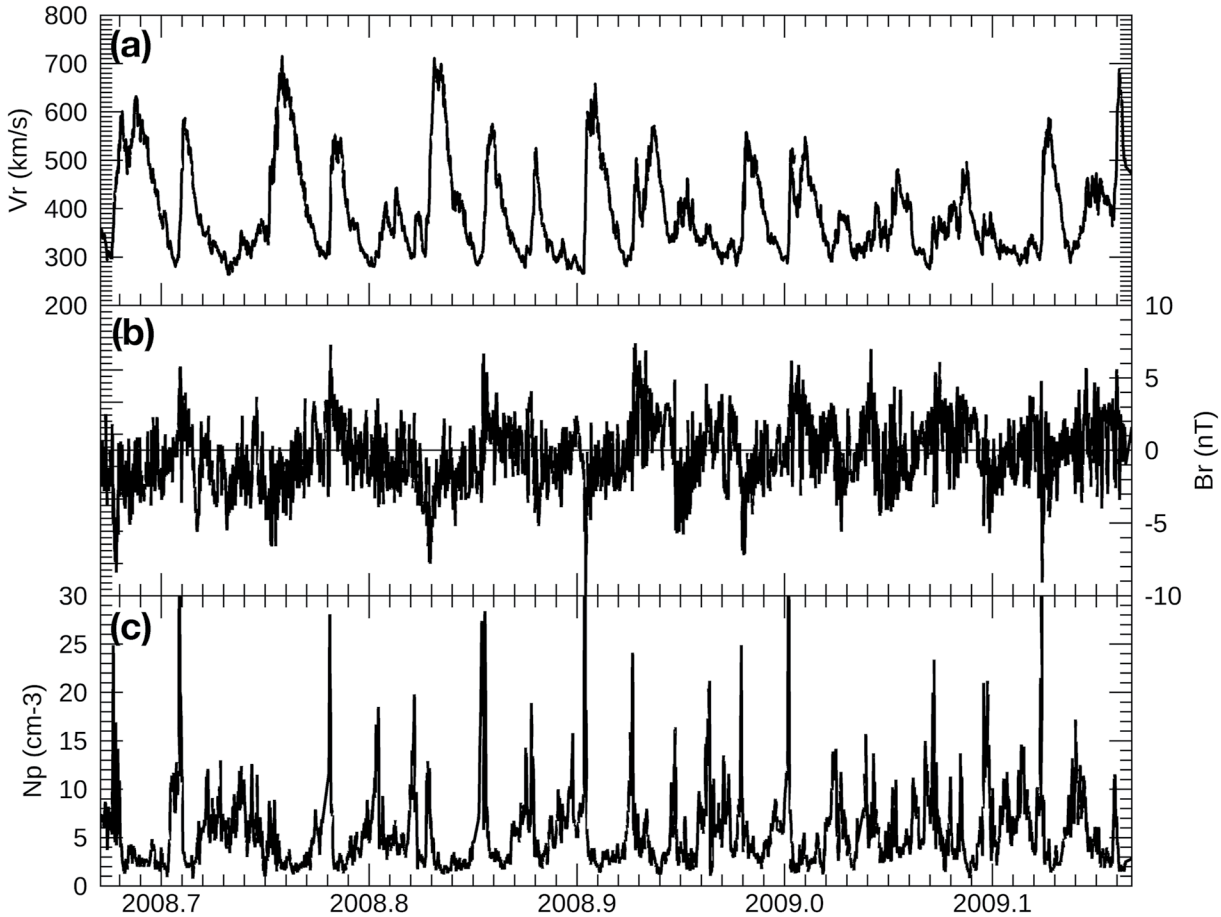

Figure 4. As Figure 3 but the solar minimum of 12/2008.

but decay during the subsequent six months. Additionally, the magnetic field shows a much clearer periodicity, apparently because of the lower levels of high-frequency fluctuations, which tended to mask the large-scale variations in the previous minimum. Next, the peak plasma densities, while occasionally reaching 30 cm^{-3}, are generally much lower. Finally, the base speeds and densities are consistently lower during this interval than the previous minimum, consistently dropping below 300 km s^{-1} and 1 cm^{-3}.

The last minimum, bracketed by the interval from 09/2019 through 03/2020, is summarized in Figure 5. Again, the recurrent streams are visible as peaks in velocity, which sweep up solar wind creating the spikes in the number density measurements. The radial field shows a general 27-day, two-sector pattern, but, as with the 22/23 minimum, it is masked by a significant "noise" component. The base velocity and density appear to be larger than the 2008 minimum, but likely not as high as the 1996 minimum. Finally, the peak density values reach 30 cm^{-3} more often than the earlier minimum, but not as frequently as the 1996 minimum.

To explore the statistical properties of the solar wind during these three epochs in more detail, in Figure 6 we show histograms of solar wind speed, radial magnetic field, and number density. The qualitative inferences we drew earlier are reinforced; however, now we can make quantitative statements about the changes from one rotation to the next. Care must be taken when interpreting these distributions, however. During the plasma's passage to 1 AU it has undergone substantial evolution. Specifically, initially slow solar wind may have been accelerated by faster wind behind it; a result of the rotation of the Sun placing parcels of plasma of different speeds along the same radial trajectory. In the process, the initially faster solar wind is slowed down. Similarly, fast solar wind accelerates away from following slower wind, creating a rarefaction region (or expansion wave) connecting the two. Where fast wind attempts to overtake slower wind, compression of the plasma results leading to higher densities and magnetic field strengths. The net effect is that the speed profile that would have been observed at

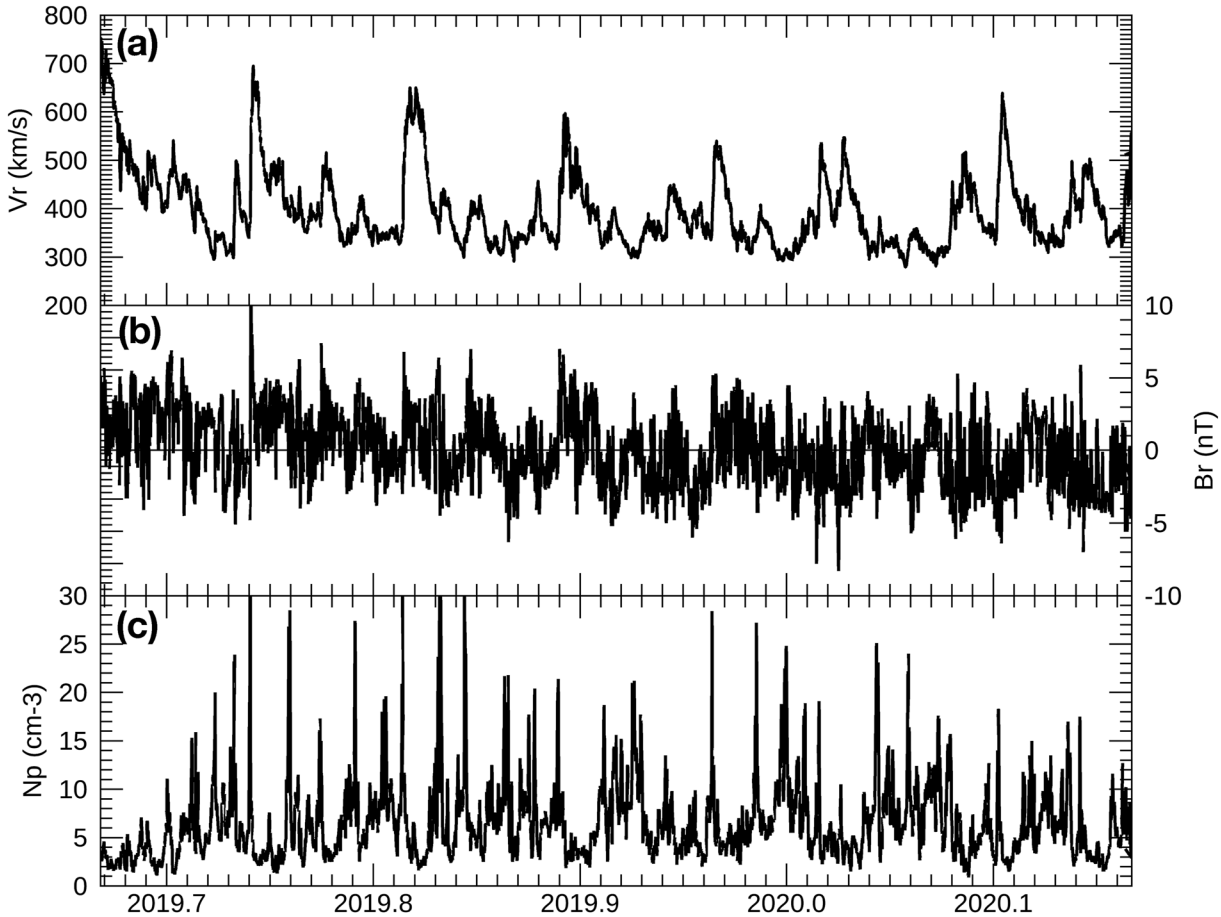

Figure 5. As Figure 3 but the solar minimum of 12/2019.

$30R_S$ is substantially modified by 1 AU. We should also take care in relating features within each histogram to one another. In particular, the slowest solar wind in (a) is not the same plasma as the lowest densities in (c). Generally, these two variables are negatively correlated.

To identify and separate parcels of plasma that remain unprocessed from those that have evolved, it is useful to consider an initial two-state solar wind, with fast, tenuous wind emanating from deep within coronal holes, and

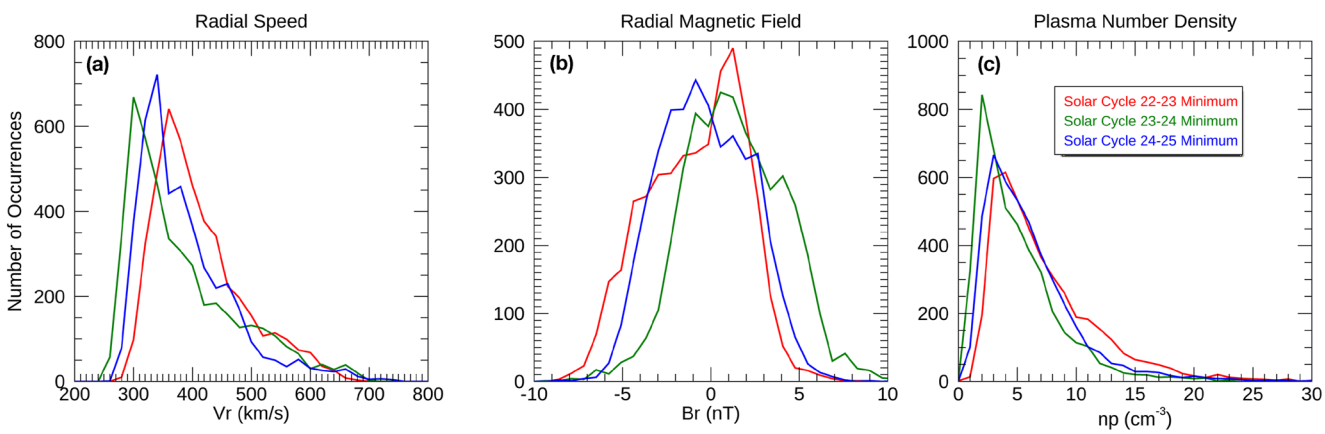

Figure 6. Histograms of ((a) solar wind speed (v_r), (b) radial magnetic field (B_r), and (c) plasma number density (N_p) for each of the three last solar minima: 08/1996 (red), 12/2008 (green), and 12/2019 (blue).

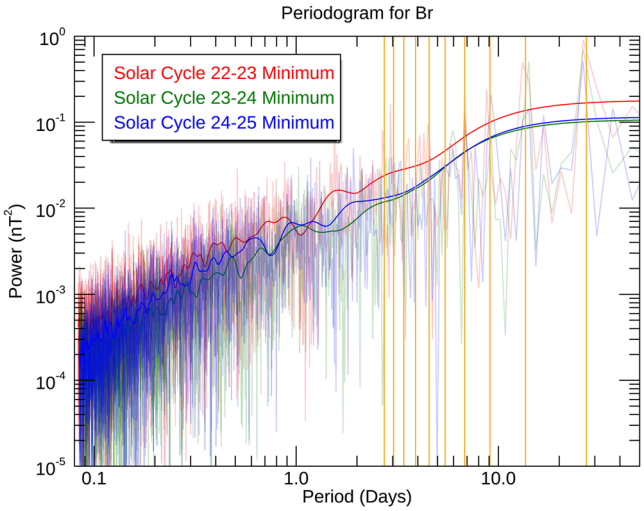

Figure 7. Power spectra for the radial component of the magnetic field for 6 month intervals surrounding each of the last three solar minima: 08/1996 (red), 12/2008 (green), and 12/2019 (blue). The jagged curves are simple, non-averaged FFT spectra, while the smooth curve includes a Tukey filter. The vertical yellow lines mark the fundamental frequency of $(27.27\ \text{days})^{-1}$ and the next nine harmonics. The data terminate at the Nyquist frequency, 1/(2 hr).

slow, dense, and more variable solar wind emanating from near the boundaries of the holes. Based on this picture, it is likely that the left most portion of the speed histograms represents slow, relatively unprocessed solar wind, while the left-most portion of the density histogram represents high-speed, tenuous and unprocessed wind. This provides a unique and reasonably robust way to assess the intrinsic differences in the properties of the two types of solar wind during the three minima. Considering first solar wind speed, we note that the left-most sharp rise in speed for the three minima is separated by 20 km s^{-1} from one minimum to the next. That is, in moving from the 22/23 minimum to the 24/25 minimum, the speed decreases by 20 km s^{-1}. Then from the 24/25 minimum to the 23/24 minimum, it decreases by another 20 km s^{-1}. Stated another way, the base or 'floor' in solar wind speed seems to have dropped by 40 km s^{-1} between the 1996 and 2008 minima, then rose modestly by 20 km s^{-1} for the 2019 minimum. Unfortunately, the highest speeds portion of the curves does not provide enough structure to make any similar inferences. Based on the observed inverse relationship between density and velocity (either through mass or momentum conservation (e.g., Riley et al., 2001), we might also infer that the density of the slow wind increased between the 1996 and 2008 minimum, and decreased modestly for the 2019 minimum. However, inspection of the high-density tails in Figure 6c does not support this conjecture, with the 1996 minimum showing the highest densities. As noted, however, this is likely due to the processing of the solar wind, and, since the high-speed streams were more substantial during this interval, this produced larger compression regions.

Considering next, the number densities (Figure 6c), the sharp rises on the left-most side of the profiles suggest a total average difference in the base densities of the fast solar wind of ~1.5 cm^{-3}, again, with the decrease occurring from the 1996 minimum to the 2008 minimum, then a rise approximately half for the 2019 minimum.

Unfortunately, it's not possible to make comparable inferences for the radial field. While it is true that the pattern is analogous, with the 1996 minimum being the broadest, the 2008 minimum being the narrowest, and the 2019 being somewhere between, there are likely asymmetries due to non-dipolar contributions to the coronal magnetic field that are shifting the distributions to one side or the other of the zero value. Additionally, it is worth remarking that there is a substantial offset in the 23–24 minimum distribution (green) compared to either the previous or following minima. In summary, based on the comparisons of solar wind speed and density, we infer that the 2008 minimum was truly a substantially new 'low' for the heliosphere, while the 2019 minimum appears to represent a partial recovery.

The variation in the strength of the three minima can also be inferred from power spectra of the *in-situ* measurements. Figure 7a periodogram—compares the power spectral density for B_r for each of the three minima as a function of period (1/frequency). The semi-transparent jagged curves are simple FFT spectra with no averaging, while the smooth solid curves have been Tukey filtered. These data are 1-hr averaged so the data terminate at the Nyquist frequency of 1/(2 hr), or $\sim 1.4 \times 10^{-4}$ Sec. Focusing first on the Tukey filtered profiles, we note that at essentially all frequencies, there is more power for the cycle 22/23 minimum. The lowest power is consistently during the 23/24 minimum. The 24/25 minimum lies on top of the 23/24 minimum for periods above 2 days; however, for periods less than this, it generally lies between the 22/23 and 23/24 minima. This can also be seen at specific frequencies, and, in particular, the rotation period of the Sun (27.27 days as viewed from Earth) as well as the first nine harmonics above this (yellow vertical lines). In most cases, the 22/23 (red) minimum has the strongest power at the solar rotation period, suggesting that structure remained present and relatively unchanged for longer periods, that is, there were more co-rotating features. Stated another way, the presence of more transient equatorial coronal holes, during the latter two minima, likely led to these intervals having less recurrent structure.

As a final and broader exploration of solar wind structure over the past three decades, we consider mass and momentum flux. The inferred solar-rotation-averaged mass flux upstream of Earth for the interval spanning 1990 through mid 2019 (almost three solar cycles) is summarized in Figure 8b. For reference, the monthly-averaged SSN is reproduced in panel (a). Several points are worth noting. First, values are relatively constant over almost

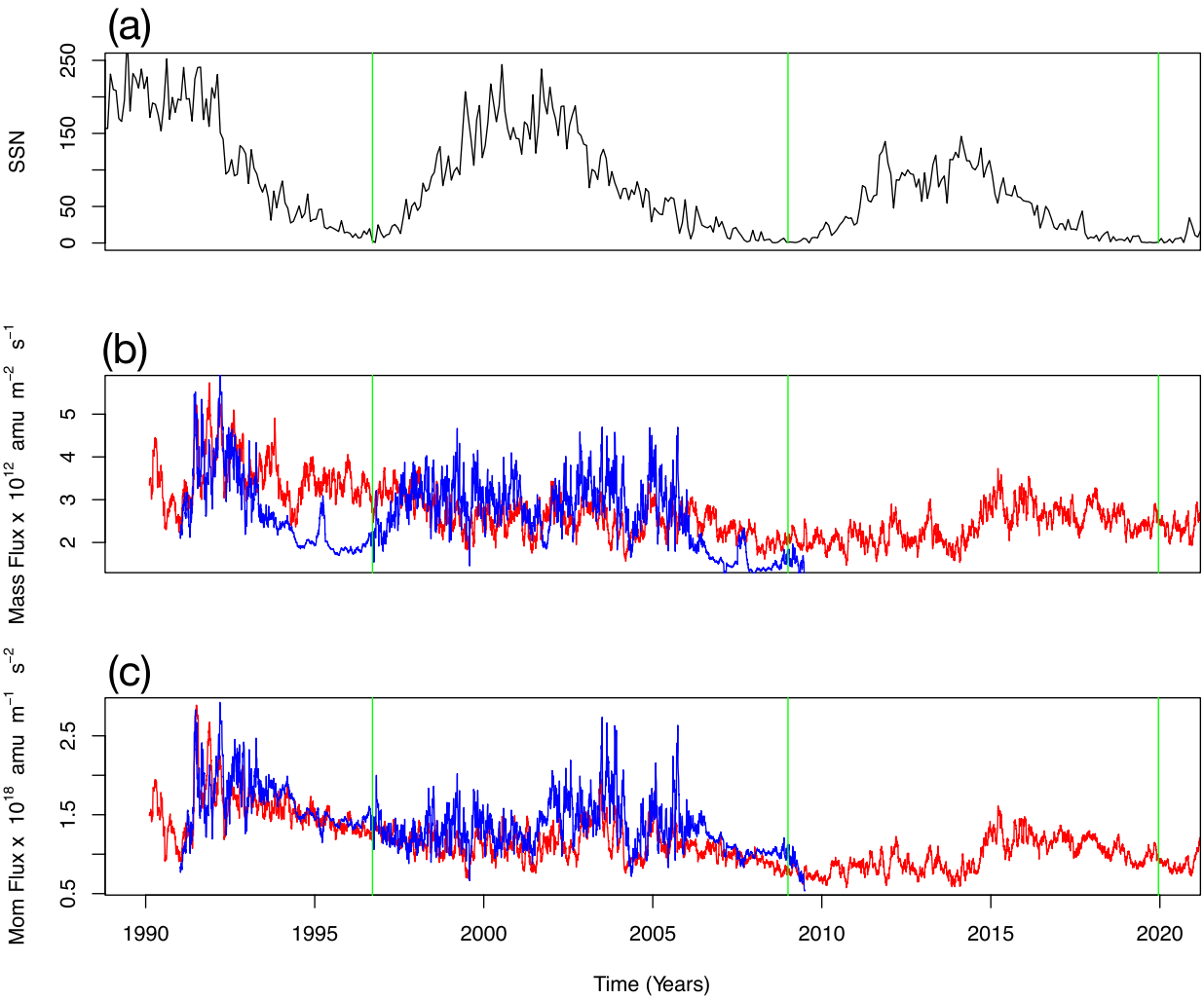

Figure 8. Time series of: (a) monthly sunspot Number (SSN) from SILSO, Royal Observatory of Belgium, Brussels; (b) Mass flux at Earth (red) and Ulysses (blue); and (c) Momentum flux estimated at Earth (red) and Ulysses (blue). The vertical green lines mark the 08/1996, 12/2008, and 12/2019 minima.

three solar cycles, ranging from ~2 to ~5 amu m^{-2} s^{-1}. Second, on the timescale of an hour, the fluctuations are much larger, driven by a range of phenomena, including waves, turbulence and other transient phenomena up to the scale of coronal mass ejections (CMEs). Third, there are no obvious large-scale variations associated with the solar cycle. For example, the solar minima in September 1996 December 2008, and December 2019, show (relatively) high, low, and high values, respectively. Similarly, the solar maxima at November 1989 (inferred from January 1990), November 2001, and April 2014, are associated with high, low, and low values, respectively. Fourth, from 1992 through 2014 there appears to be a modest but consistent decrease in value from a peak of ~5×10^{12} amu m^{-2} s^{-1} to ~2×10^{12} amu m^{-2} s^{-1}. Fifth, from 2015 through mid-2019 values have increased modestly (~3×10^{12} amu m^{-2} s^{-1}) but remained constant.

The scaled momentum flux of the solar wind upstream of Earth is shown in Figure 8c, red curve). Again, longer-period trends are apparent. From early 1990 through 2019, e.g., the flux generally decreased from almost 2×10^{18} amu m^{-1} s^{-2} to less than 1×10^{18} amu m^{-1} s^{-2}. Since 2015, it has increased modestly, but remained approximately constant through mid 2019. As with the mass flux, there is no obvious correlation with solar cycle.

The scaled mass flux at the location of Ulysses is overlaid in Figure 8b, blue curve). Similar points can be made, including the relative size of the fluctuations and the net decrease in values from 1992 through 2009. There are, however, some important differences. First, over several years surrounding early 1995 and late 2007, the size

of the fluctuations decreased significantly. These correspond to Ulysses' immersion within the high-latitude, high-speed, quiescent solar wind during near-solar-minimum conditions. The center of each of these intervals, in which the fluctuations return, is the mid-point of the rapid-latitude scan. These two intervals correspond to the first and third orbit (McComas et al., 2008). The second orbit, which occurred midway between them can be identified, but it occurred at near-solar maximum conditions, during which time there were no well-established large polar coronal holes (Riley et al., 2003). A second point worth noting is that the mass flux is not constant as a function of heliographic latitude, with polar intervals showing consistently lower values. This is apparent even during the equatorial traversals during the two rapid latitude scans at solar minima.

Finally, the scaled momentum flux of the solar wind measured at Ulysses is shown by the blue curve in Figure 8c. The match between the two profiles is remarkable. Both the absolute values and their large-scale temporal evolution track one another very well. Even at sub-year scales, the variations are often mirrored, such as the interval between 2000 and 2005. We note further that the momentum flux values dropped further until 2010, remained approximately constant until 2014, then climbed modestly in 2015, reaching a new modest peak from which it appears to be slowly receding. Finally, comparing the calculated mass and momentum flux at the three minima, we note that the values were highest in 08/1996, lowest in 12/2008, and midway between the two in 12/2019.

3.2. Model Results

Global heliospheric models rely on some estimate for the photospheric magnetic field to generate solutions for a particular interval of interest. Our MHD calculations have typically used either MDI- or HMI-derived synoptic maps as the starting point for specifying the lower radial boundary conditions for the coronal model. These are summarized in Figure 9 for CRs 1912 (07/25/1996 to 08/22/1996), 2077 (11/20/2008 to 12/17/2008), and 2224 (11/12/2019 to 12/10/2019). To facilitate a better comparison, the contours have been saturated at ±20 G. Comparing the three panels, we note several points. First, the polar field strengths are notably larger for 1912 than either 2077 or 2224. This is consistent with the inferences drawn from the data in Figure 2. It should be noted, however, in deriving these maps, the polar regions must be filled in using an extrapolation procedure. Thus, quantitative comparisons between them are probably less valuable than the results inferred directly from WSO observations (FIgure 2b). Second, there are more active regions in 1912, and their strengths are also greater. Third, the 22-year Hale cycle is reflected by the reversal from positive northern pole, to negative, and back to positive for each of the three minima. In terms of specific structure, we note that both 1912 and 2224 are dominated by ARs at ∼270° longitude, while 2077 has two ARs, both in the northern hemisphere and located at ∼180° and ∼245° longitude. In summary, Carrington Rotation (CR) 1912 appears to be significantly different in a number of important respects than either 2077 or 2224.

In Figure 10 we show the computed coronal-hole boundaries from the coronal solutions for each of the solar minima. These were calculated by tracing along field lines from the base of the corona and identifying them as open (red or blue) or closed (gray). The holes have been further color-coded according to the polarity of the underlying field (red for outward and blue for inward). CR 1912 (and 1913) were well-studied as part of the WSM interval and the so-called "elephant's trunk" extension of the northern polar coronal hole at ∼270−300° longitude is one of the "classic" features of this interval. Additional excursions toward the equator are visible but, with perhaps a modest exception, there are no substantial equatorial coronal holes. For CRs 2077 and 2224, on the other hand, there are both more equatorial and mid-latitude coronal holes (i.e., holes that were not connected to a polar coronal hole) as well as more structure/penetration into the lower latitude regions.

As noted in Section 2, a hybrid approach is employed to drive the heliospheric model, where the magnetic structure of the corona is used to develop the inner radial boundary speed profiles. These have been shown to produce solar wind at 1 AU, that more closely matches the observations (Riley et al., 2001, 2020; Riley, Linker, Lionello, & Mikic, 2012). The velocity maps for each of the solar minimum Carrington rotations are shown in Figure 11. Considering first the similarities between each of the panels, we note that fast, uniform flow dominates most of the spherical domain. It is only within a relatively modest "band of solar wind variability" (Gosling et al., 1995) that there is any structure in the speed of the solar wind. Of course, this is where Earth is located and is thus of paramount importance. In general, this slow flow band encapsulates the HCS (white line), and the band of variability is roughly centered about it. Additionally, there is considerable structure at the boundary between slow (blue) and fast (red) wind, with a "boundary region" of increasing speed joining the two. Back at the base of the corona, this is a smooth and very narrow strip that traces along the edge of the open closed field regions, and

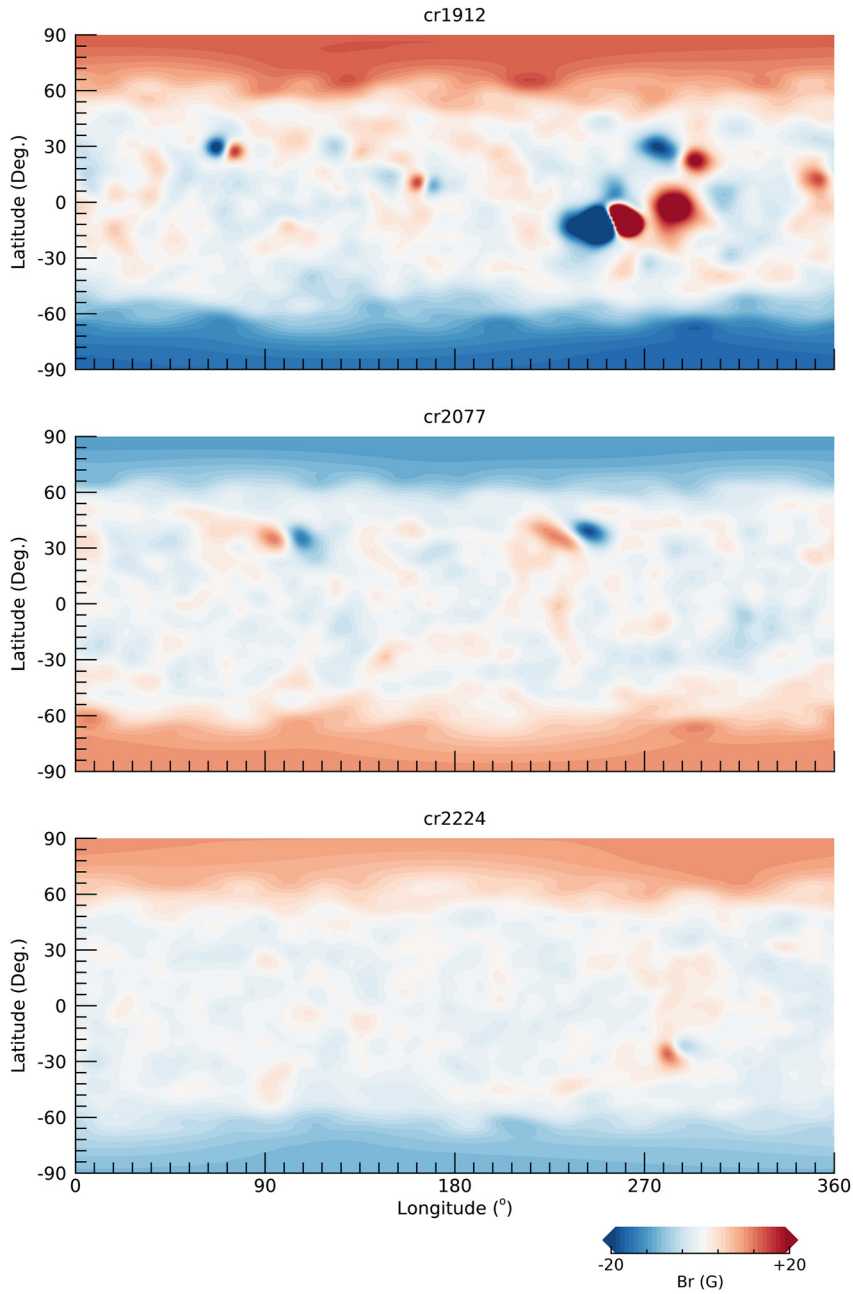

Figure 9. Radial magnetic field input boundary conditions for CR (a) 1912, (b) 2077, and (c) 2224 derived from synoptic maps from MDI (a) and HMI (b) and (c). For better comparison between epochs, the panels have been saturated to the ±20 G in all cases.

acts as a proxy for mechanisms of solar wind release from this region, such as interchange reconnection (e.g., Riley & Luhmann, 2012). The orientation of these boundaries, as a function of longitude and latitude, can drive the development of compression and rarefaction regions. For example, the fast wind at 230° and −15° latitude in the top panel, will become radially aligned to slower wind released earlier to the west (increasing longitude). Thus, we can anticipate the formation of a compression region here, of an extent slightly larger than the length of boundary at this orientation, and, in fact, this is consistent with what is observed (e.g., Gosling et al., 1993; Riley et al., 1996; Riley, Linker, Americo Gonzalez Esparza et al., 2012).

Comparison between the velocity maps in Figure 11 and the coronal holes shown in Figure 10 allows us to infer the likely source of some of the structure in the band of solar wind variability, particularly, for the equatorward

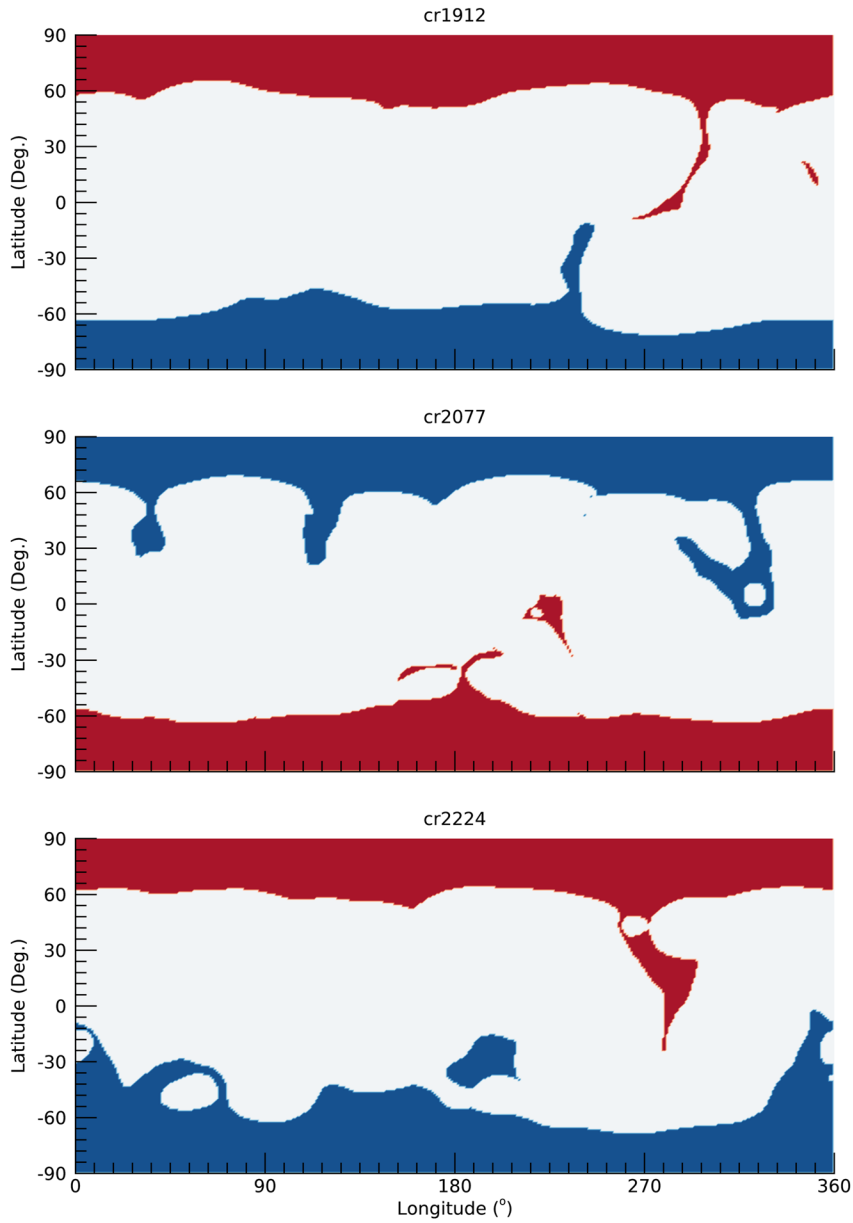

Figure 10. Computed coronal hole boundaries for CR (a) 1912, (b) 2077, and (c) 2227. Red and blue indicate regions of open magnetic field, while regions of light gray are closed magnetic field regions. Outwardly-directed open field is shown in red, and inward open field is shown in blue.

extensions of the coronal holes. A feature that is particularly evident for 2077 and 2224 is the manifestation of equatorial (or at least isolated) coronal holes, which appear as isolated regions of fast solar wind. A particularly good example of this can be seen in the 2077 map at a longitude of 230°. To a lesser extent, there are the remnants of one at 230° longitude in CR1912. In CR 2224, these high-speed regions are even more distinct, being separated on the non-HCS side by an arc of solar wind. These are regions that, back at the Sun, are associated with pseudo-streamers (Riley & Luhmann, 2012).

A final distinction worth mentioning between the velocity maps for each of the minima concerns the relative orientation and breadth of the band of solar wind variability (or equivalently, the location of the HCS) with respect to the solar equatorial plane. For 1912, the HCS is relatively flat for the longitudinal range: $60° < \phi < 170°$, before undergoing substantial latitudinal swings, which are mirrored in an initially confined and flat band of slow wind, which then flares out to encompass a range $>\pm 35°$. For 2077, the slow-flow band remains within $\sim\pm 25°$ of the

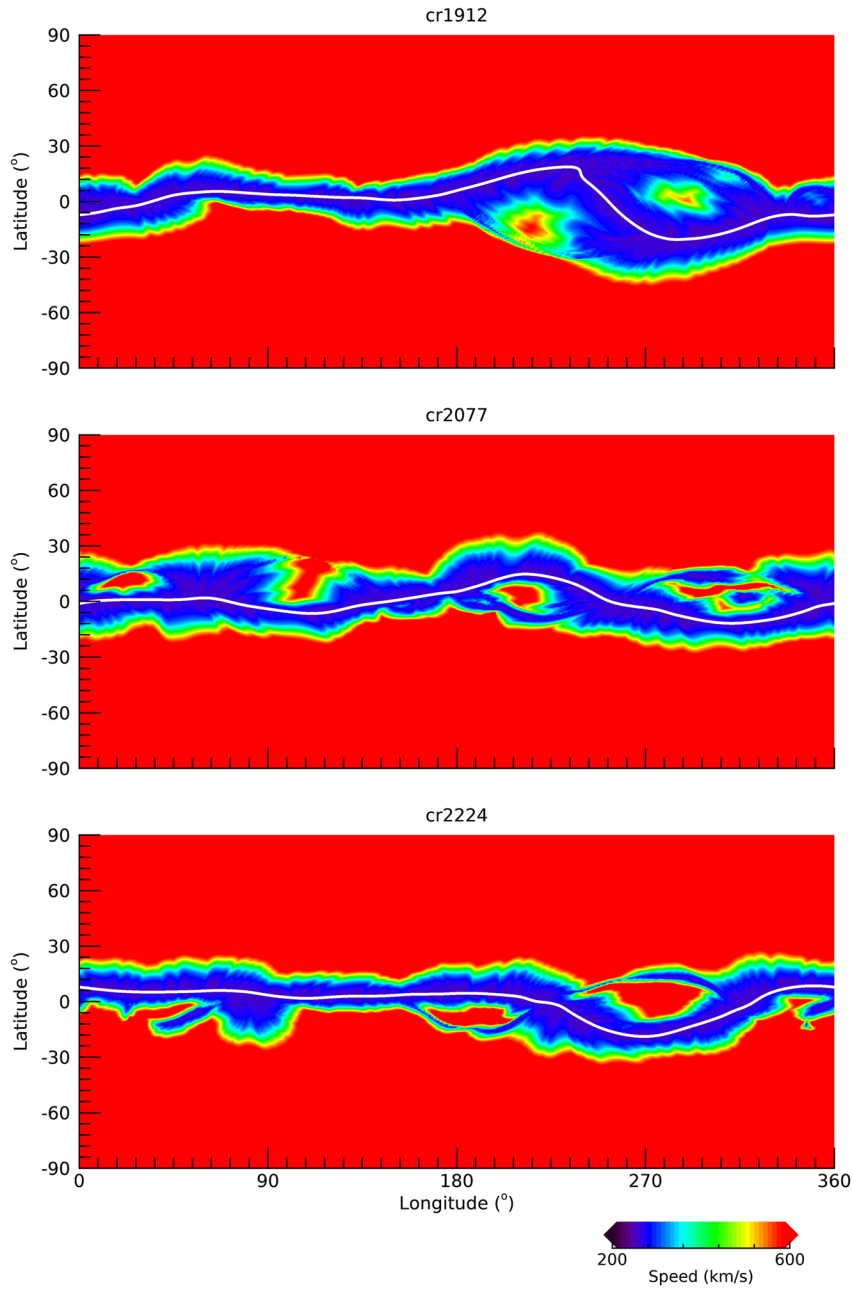

Figure 11. Modeled radial velocity profiles for CRs 1912, 2077, and 2224 at $30R_S$. Overlaid is the location of the heliospheric current sheet, as determined by the contour of $B_r = 0$ (white curve).

location of the HCS, but tracks its position. Finally, for 2224, the band is essentially flat, and more constrained in latitude, except for a localized excursion into the southern hemisphere centered around 270°. Comparison with Figure 9 provides clues for why this is the case. For 2224, there is only one significant active region centered at 270°.

As the solar wind propagates through the heliosphere, the patterns shown in Figure 11 evolve in a predictable way. Compression regions form where faster wind at the same latitude follows (i.e., lies to the east of) slower wind. In contrast, expansion waves (rarefaction regions) form where fast wind lies to the west of slower wind (Figure 12). Additionally, the HCS is deformed. A good example of this is the northern excursion of the HCS during CR 2077 at ∼235° longitude in Figure 11. At 1 AU, the entire pattern has drifted eastward (in Carrington coordinates) such that the same features lies at ∼165° longitude. Note, however, that the west side of the HCS has steepened,

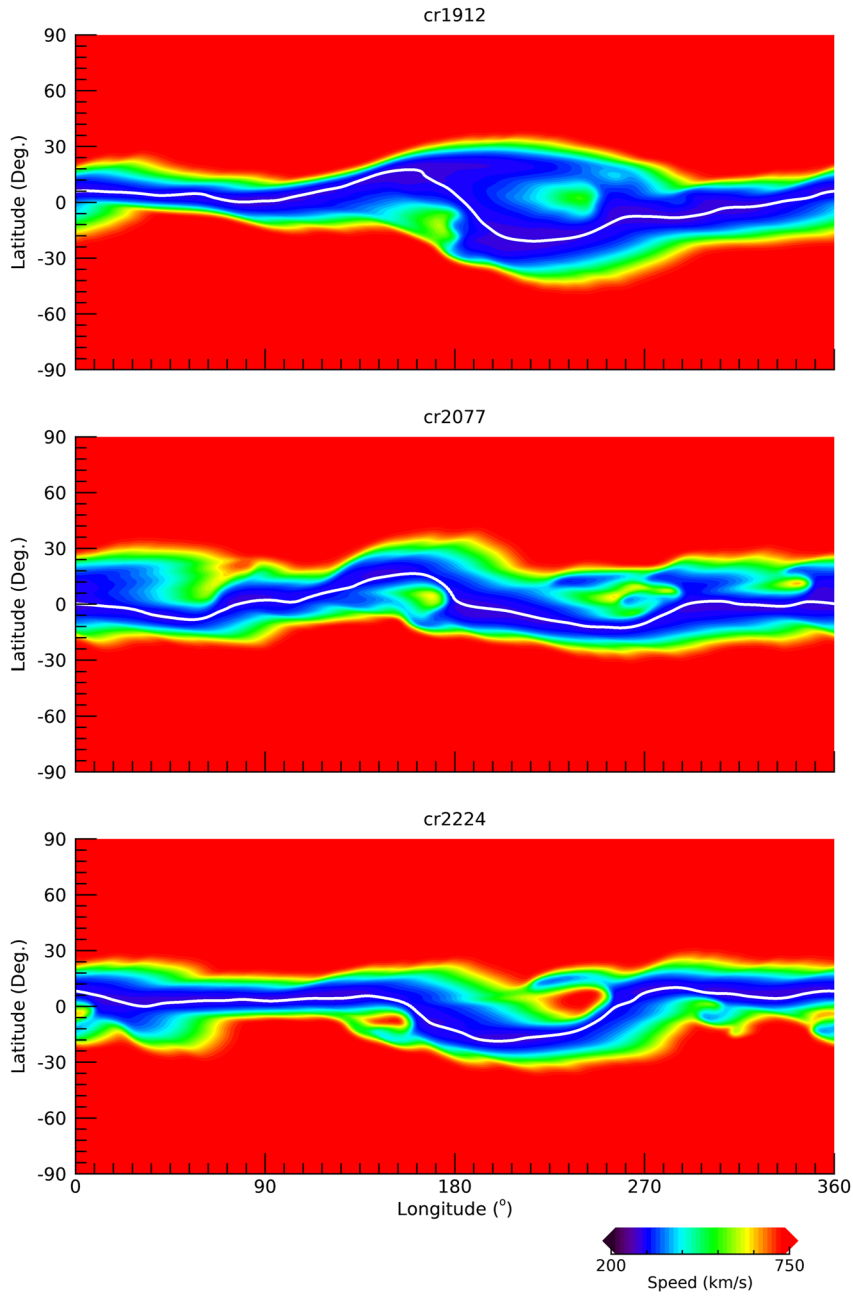

Figure 12. Modeled radial velocity profiles for CRs 1912, 2077, and 2224 at 1 AU. Overlaid is the location of the heliospheric current sheet, as determined by the contour of $B_r = 0$ (white curve).

whereas the eastern side has become more shallow, with respect to latitude. This reflects the dynamical stretching by the equatorial coronal hole that created the deformation, broadening the region to the east and compressing it to the west. Such effects (although less pronounced) can be seen elsewhere during all three intervals.

Finally, we can make a statistical comparison of the model results with the *in-situ* measurements. In Figure 13, we make a comparable model-based histogram comparing speed, field, and density. In general, the distribution in the parameters compares favorably with the observations. However, while we inferred that the observed floor in solar wind speed changed in each minimum, as did the floor in density, our model has a fixed floor in both speed and density for all three minima. This is easily understood because, for the semi-empirical model, these numbers are free parameters that are set. And, in fact, these were optimized (or tuned) for the 1996 minima. In principle,

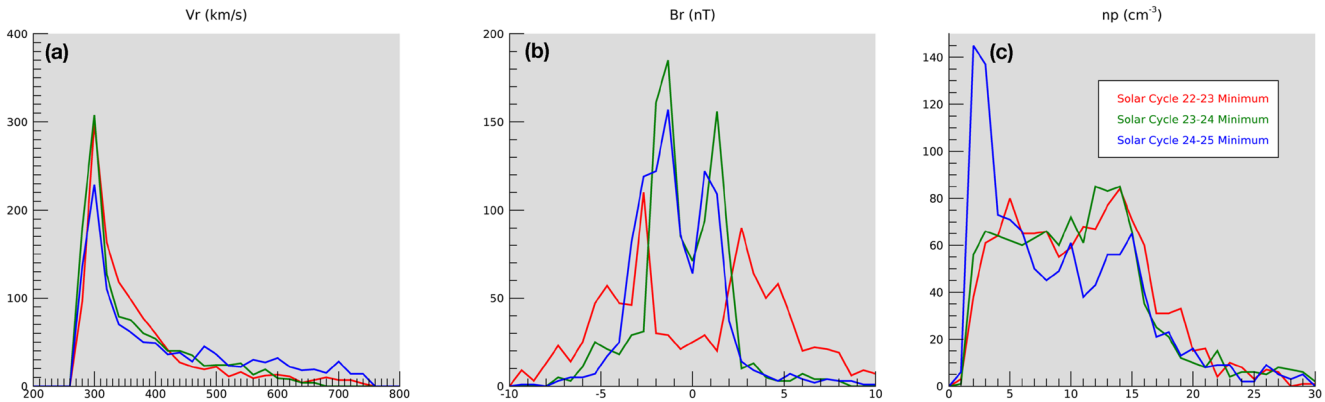

Figure 13. Histograms of modeled (a) solar wind speed (v_r), (b) radial magnetic field (B_r), and (c) plasma number density (N_p) for each of the three last solar minima: 08/1996 (red), 12/2008 (green), and 12/2019 (blue).

we could re-run a set of model comparisons for each of the subsequent minima and identify parameters that would lead to better matches with the observations. And, for space weather applications, this might be a reasonable exercise. However, from the perspective of scientific understanding, a more sophisticated model that can naturally produce these varying floors in the plasma and magnetic field parameters is considerably more desirable.

4. Summary and Discussion

In this study, we have compared the properties of the three most recent solar minima using remote solar observations, *in-situ* measurements, and MHD models. Observationally, we found that solar indices suggested a more systematic slide to evermore quiescent conditions, as exemplified by the reduction in peak sunspot number values and longer duration of a "floor" at solar minimum. On the other hand, the statistical properties of the solar wind, as inferred from *in-situ* measurements at 1 AU suggested that the most recent minimum (12/2019) reflected a partial return to values measured during the 08/1996 minimum. Global MHD simulation results for Carrington rotations corresponding to each of these minima suggested that the two most recent minima were structurally more similar to one another than to the 1996 minimum, driven primarily by the presence of equatorial coronal holes, and, thus, associated with the presence of pseudo-streamers. Although the model results provide a global context for interpreting both the remote solar observations and *in-situ* measurements, the comparison also reveals several limitations in the model results, which can be addressed in future studies.

Our results are generally consistent with previous studies investigating the similarities and differences of the solar minima of 1996 and 2008. McComas et al. (2008), for example, demonstrated that the solar wind measured at Ulysses over the polar regions in the months prior to the 2008 minimum was slightly slower but notably more tenuous and cooler than the wind measured during the 1996 minimum. In contrast, at 1 AU and in the ecliptic plane, the average speed of the solar wind increased from the 1996 minimum to the 2008 minimum (Gibson et al., 2009; Lee et al., 2009; Owens et al., 2008). It must be emphasized, however, that these studies did not compare measurements at the same epochs in the solar cycle: While the 1996 data were representative of the minimum at that time, the 2008 dataset was based on data from the early portion of 2008, in spite of the fact that the minimum was not finally established as having occurred in December of that year. Thus, the higher speeds inferred for this second minimum were likely the results of sampling the solar wind during the late declining portion of the cycle, when there remained a more substantial tilt to the dipolar component of the field, and, thus, more sampling of polar coronal holes by the near-Earth spacecraft. Simulation studies comparing these two epochs were generally consistent with the current results, including the presence of pseudo-streamers (Riley & Luhmann, 2012) and structure and properties of CIRs (Riley, Linker, Americo Gonzalez Esparza et al., 2012; Riley, Linker, Lionello, & Mikic, 2012). Again, in retrospect, these comparative studies also suffered from the premature analysis of conditions appropriate for the 12/2008 minimum.

Our results can be broadly interpreted with the basic picture of how the corona is heated and the solar wind is accelerated. Riley et al. (2010), for example, used the results of McComas et al. (2008) to infer a linear relationship between proton number density and radial magnetic field strength in the high-speed solar wind. They also

demonstrated a correlation between photospheric magnetic field measurements and the strength of the interplanetary magnetic field. Coupling these observational constraints with results from simulation results, which suggested a linear relationship between the coronal heating rate and number density in the solar wind, suggests that heating rate within coronal holes scales linearly with the open unsigned magnetic flux. Comparison of Figures 2 and 6 generally support this. From the 1996 to 2008 minimum, the polar field strength dropped substantially. The lowest measured densities in the solar wind (reflecting the high-speed polar plasma) also dropped significantly. Then from the 2008 to 2019 minimum, the polar fields - arguably - increased modestly (Figure 2b), and the *in-situ* densities also increased.

Our model relied on a number of assumptions and approximations that require qualification. First, we employed an empirical approach, the DCHB technique to derive the speed profiles used to drive the heliospheric model (Riley et al., 2001). As we have noted previously, this is also substantially similar to the current implementation of the Wang-Sheeley-Arge (WSA) model that is used in a number of space weather applications (e.g., Riley, Linker, and Arge (2015)). It must be recognized that both the DCHB and WSA techniques contain several free parameters that are used to set base values for the slow and fast solar wind. Here, we have shown that, while they were optimized for the 1996 minimum, they are likely not well tuned for the following two minima (see and compare Figures 6 and 13). A revised model should be developed that attempts to adjust these parameters to facilitate better matches for the 2008 and 2019 minima. Of course, a better option, and one that we are actively pursuing, is to implement a model that self-consistently produces solar wind values that match observations, driven by the observed changes in the photospheric magnetic field that have occurred over the last three decades (Downs et al., 2016; Mikić et al., 2018b).

Second, and related to this first point, global heliospheric space weather models, such as operated at NOAA's Space Weather Prediction Center (Pizzo et al., 2011), typically rely on either conservation of mass or momentum flux to derive a relationship between density and radial velocity, which necessary to fully prescribe the inner boundary conditions of heliospheric portion of the simulation (e.g., Riley, Lionello, et al., 2012; Riley, Linker, Americo Gonzalez Esparza et al., 2012). For example, PSI's CORona-HELiosphere (CORHEL) model assumes momentum flux conservation (Riley et al., 2001) to estimate density (given a velocity profile and a "base" density value). In contrast, the Hybrid Heliospheric Modeling System developed by Detman et al. (2006) enforces mass conservation to derive the number density at the boundary. Our results suggest that mass conservation is a poor assumption to make. It is not well conserved as a function of latitude, nor is it well-conserved over time (varying by up to a factor of two under near-solar minimum conditions). Moreover, there appears to have been a significant decrease for the last two solar cycles. Momentum flux conservation, on the other hand, appears to be a more reasonable assumption. Nevertheless, there are two important caveats: (a) latitudinally, polar values may be 10%–15% larger than their equatorial counterparts; and (b) on the timescale of a solar cycle, the overall value of the momentum flux may vary by up to 50%. It is possible that these temporal variations can be accounted for by simply adjusting the "base" density parameter in the model, such that it tracks the evolution in momentum flux. However, addressing the latitudinal variations, while not critical for space weather applications, would require a more general description of the momentum flux over the inner radial boundary sphere. As discussed below, however, a better solution would be to address the mismatch with a more physics-based, self-consistent model.

Third, our model does not explicitly include time dependent effects. Although the DCHB approximation attempts to mimic theories that naturally produce a boundary layer of slow and variable solar wind at the boundary between open and closed fields, such as the so-called "interchange reconnection" model (Fisk et al., 1998), it does so empirically. To address this in any fundamental way requires the explicit treatment of time-varying photospheric magnetic fields, driving sporadic reconfigurations of the magnetic field.

Fourth, our model solutions necessarily rely on boundary conditions derived from Earth-based magnetic observatories. To generate a pseudo-synoptic map, data outside of this field of view are measurements that were taken while the region was in the field of view and differentially rotated to their new position. The resultant maps are then "diachronic" and not "synchronic" (Riley et al., 2014), which are strictly necessary for a global model. Flux transport models, such as Air Force Data Assimilative Photospheric Flux Transport (ADAPT) attempt to mitigate these limitations by including various data assimilation techniques, together with a photospheric magnetic flux transport model. To fully resolve this issue, however, would require the development of truly synchronic maps assembled from simultaneous observations from multiple spacecraft, including views of the polar regions

(Riley et al., 2019). Although such mission concepts have been, and continue to be evaluated, none, so far have been successful.

Our results suggest several primary areas for future study. For example, while solar indices suggest that the two most recent minima (2008 and 2019) were notably more subdued the earlier ones of the space era, solar wind parameters hint that the last minimum was, in some ways, a partial recovery. This is further supported by the recent increase in solar activity during the rising phase of solar cycle 25. Thus, it would be valuable to investigate other descriptors of solar activity, which might provide further clues about whether we are continuing toward a grand minimum, such as the Dalton minimum, or whether we are climbing out of a brief minimum period and returning to activity levels that are more indicative of the early space era. Answering this question will be of considerable value for space weather applications.

A second important area for study lies in addressing the current main limitations of the global models: (a) improving the quasi-synchronic maps used to drive the model; (b) assessing and improving the accuracy of more sophisticated global MHD models; and (c) incorporating the time-dependence as a basic component of the model solutions.

In closing, we reiterate the main points of this study, that: (a) while solar indices suggest that the intervals surrounding the two most recent minima were similar to one another, but significantly less active than the earlier minimum (1996), solar wind parameters suggest that the last minimum represents a partial recovery; and (b) global models, while limited in several important respects, are able to reconstruct, and provide a global context for interpreting *in-situ* measurements and connect them to their solar sources.

Data Availability Statement

All data and model results analyzed in this study are publicly available. Photospheric magnetic field observations were obtained from the Joint Science Operations Center (JSOC, http://jsoc.stanford.edu/). All in situ data were obtained from NASA's Space Physics Data Facility (SPDF) web services API (https://spdf.gsfc.nasa.gov/). Model results can be obtained from PSI's modeling website (www.predsci.com).

Acknowledgments
The authors gratefully acknowledge support from NASA (80NSSC18K0100, NNX16AG86G, 80NSSC18K1129, 80NSSC18K0101, 80NSSC20K1285, 80NSSC18K1201, and NNN06AA01C), NOAA (NA18NWS4680081), and the U.S. Air Force (FA9550-15-C-0001). The authors also appreciate the efforts of NASA's Space Physics Data Facility (SPDF) for developing easy-to-use APIs for accessing data from past and present missions.

References

Candey, R., Bilitza, D., Chimiak, R., Cooper, J., Garcia, L., Gladney, C., et al. (2019). Parker solar probe in-situ data at the spdf archives.

Caplan, R. M., Downs, C., & Linker, J. (2019). Preparing photospheric magnetic field measurements for use in coronal and heliospheric models. In *Agu fall meeting abstracts* (Vol. 2019). SH43E–3389.

Caplan, R. M., Linker, J. A., Mikić, Z., Downs, C., Török, T., & Titov, V. (2019). Gpu acceleration of an established solar mhd code using openacc. *Journal of Physics: Conference Series*, *1225*, 012012. https://doi.org/10.1088/1742-6596/1225/1/012012

Clette, F., & Lefèvre, L. (2016). Wdc-silso: A full modernization of the multi-century sunspot record.

Detman, T., Smith, Z., Dryer, M., Fry, C. D., Arge, C. N., & Pizzo, V. (2006). A hybrid heliospheric modeling system: Background solar wind. *Journal of Geophysical Research*, *111*, 7102. https://doi.org/10.1029/2005JA011430

De Toma, G., White, O. R., & Harvey, K. L. (2000). A picture of solar minimum and the onset of solar cycle 23. i. global magnetic field evolution. *The Astrophysical Journal*, *529*(2), 1101–1114. https://doi.org/10.1086/308299

Downs, C., Lionello, R., Mikić, Z., Linker, J. A., & Velli, M. (2016). Closed-field coronal heating driven by wave turbulence. *The Astrophysical Journal*, *832*(2), 180. https://doi.org/10.3847/0004-637x/832/2/180

Ebert, R. W., McComas, D. J., Elliott, H. A., Forsyth, R. J., & Gosling, J. T. (2009). Bulk properties of the slow and fast solar wind and interplanetary coronal mass ejections measured by Ulysses: Three polar orbits of observations. *Journal of Geophysical Research*, *114*, 1109. https://doi.org/10.1029/2008JA013631

Eddy, J. A. (1976). The maunder minimum. *Science*, *192*, 1189–1202. https://doi.org/10.1126/science.192.4245.1189

Finsterle, W., Montillet, J. P., Schmutz, W., Šikonja, R., Kolar, L., & Treven, L. (2021). The total solar irradiance during the recent solar minimum period measured by soho/virgo. *Scientific Reports*, *11*(1), 1–10. https://doi.org/10.1038/s41598-021-87108-y

Fisk, L. A., Schwadron, N. A., & Zurbuchen, T. H. (1998). On the slow solar wind. *Space Science Reviews*, *86*, 51–60. https://doi.org/10.1007/978-94-011-4762-0_3

Gibson, S., De Toma, J., Emery, B., Riley, P., Zhao, E., Elsworth, Y., et al. (2011). The whole heliosphere interval in the context of a long and structured solar minimum: An overview from sun to earth. *Solar Physics*. https://doi.org/10.1007/s11207-011-9921-4

Gibson, S. E., Kozyra, J. U., De Toma, G., Emery, B. A., Onsager, T., & Thompson, B. J. (2009). If the sun is so quiet, why is the earth ringing? A comparison of two solar minimum intervals. *Journal of Geophysical Research*, *114*, 9105. https://doi.org/10.1029/2009JA014342

Gosling, J. T., Bame, S. J., Feldman, W. C., McComas, D. J., Phillips, J. L., Goldstein, B. E., et al. (1995). The band of solar wind variability at low heliographic latitudes near solar activity minimum: Plasma results from the Ulysses rapid latitude scan. *Geophysical Research Letters*, *22*(23), 3329–3332. https://doi.org/10.1029/95gl02163

Gosling, J. T., Bame, S. J., McComas, D. J., Phillips, J. L., Pizzo, V. J., Goldstein, B. E., & Neugebauer, M. (1993). Latitudinal variation of solar wind corotating stream interaction regions: Ulysses. *Geophysical Research Letters*, *20*(24), 2789–2792. https://doi.org/10.1029/93gl03116

Harvey, K. L., & White, O. R. (1999). What is solar cycle minimum? *Journal of Geophysical Research*, *104*(A9), 19759–19764. https://doi.org/10.1029/1999ja900211

Hoeksema, J. (1984). *Structure and evolution of the large-scale solar and heliospheric magnetic fields: PhD thesis*. Stanford University. Publication date: 09/1984.
Hoeksema, J. (1992). Large-scale structure of the heliospheric magnetic field: 1976-1991. In *Solar wind seven* (pp. 191–196). Elsevier. https://doi.org/10.1016/b978-0-08-042049-3.50042-9
Hoeksema, J. T., Wilcox, J. M., & Scherrer, P. H. (1983). The structure of the heliospheric current sheet: 1978-1982. *Journal of Geophysical Research*, *88*, 9910–9918. https://doi.org/10.1029/ja088ia12p09910
Kirk, M. S., Pesnell, W. D., Young, C. A., & Hess Webber, S. A. (2009). Automated detection of EUV polar coronal holes during solar cycle 23. *Solar Physics*, *257*, 99–112. https://doi.org/10.1007/s11207-009-9369-y
Lee, C. O., Luhmann, J. G., Zhao, X. P., Liu, Y., Riley, P., Arge, C. N., et al. (2009). Effects of the weak polar fields of solar cycle 23: Investigation using OMNI for the STEREO mission period. *Solar Physics*, *256*, 345–363. https://doi.org/10.1007/s11207-009-9345-6
Lionello, R., Linker, J. A., & Mikić, Z. (2001). Including the transition region in models of the large-scale solar corona. *The Astrophysical Journal*, *546*, 542–551. https://doi.org/10.1086/318254
Lionello, R., Linker, J. A., & Mikić, Z. (2009). Multispectral emission of the sun during the first whole sun month: Magnetohydrodynamic simulations. *The Astrophysical Journal*, *690*, 902–912. https://doi.org/10.1088/0004-637X/690/1/902
McComas, D. J., Bame, S. J., Barker, P., Feldman, W. C., Phillips, J. L., Riley, P., & Griffee, J. W. (1998). Solar wind electron proton alpha monitor (swepam) for the advanced composition explorer. *SSR*, *86*(1/4), 563–612. https://doi.org/10.1007/978-94-011-4762-0_20
McComas, D. J., Barraclough, B. L., Funsten, H. O., Gosling, J. T., Santiago-Muñoz, E., Skoug, R. M., et al. (2000). Solar wind observations over Ulysses' first full polar orbit. *Journal of Geophysical Research*, *105*, 10419–10433. https://doi.org/10.1029/1999JA000383
McComas, D. J., Ebert, R. W., Elliott, H. A., Goldstein, B. E., Gosling, J. T., Schwadron, N. A., & Skoug, R. M. (2008). Weaker solar wind from the polar coronal holes and the whole Sun. *Geophysical Research Letters*, *35*, 18103. https://doi.org/10.1029/2008GL034896
McComas, D. J., Elliott, H. A., Gosling, J. T., & Skoug, R. M. (2006). Ulysses observations of very different heliospheric structure during the declining phase of solar activity cycle 23. *Geophysical Research Letters*, *33*, 9102. https://doi.org/10.1029/2006GL025915
Mikić, Z., Downs, C., Linker, J. A., Caplan, R. M., Mackay, D. H., Upton, L. A., et al. (2018a). Predicting the corona for the 21 august 2017 total solar eclipse. *Nature Astronomy*, *1*.
Mikić, Z., Downs, C., Linker, J. A., Caplan, R. M., Mackay, D. H., Upton, L. A., et al. (2018b). Predicting the corona for the 21 august 2017 total solar eclipse. *Nature Astronomy*, *1*.
Mikić, Z., & Linker, J. A. (1994). Disruption of coronal magnetic field arcades. *The Astrophysical Journal*, *430*, 898. https://doi.org/10.1086/174460
Mikic, Z., Lionello, R., Downs, C., Linker, J. A., Riley, P., Shen, C., & Raymond, J. (2018). Investigating modeled ion charge states in the solar wind during the 21 august 2017 total solar eclipse. In G. Lapenta (Ed.), *Solar wind 15*. AIP.
Ogilvie, K. W., Chornay, D. J., Fritzenreiter, R. J., Hunsaker, F., Keller, J., Lobell, J., et al. (1995). Swe, a comprehensive plasma instrument for the wind spacecraft. *Space Science Reviews*, *71*, 55–77. https://doi.org/10.1007/bf00751326
Owens, M. J., Crooker, N. U., Schwadron, N. A., Horbury, T. S., Yashiro, S., Xie, H., et al. (2008). Conservation of open solar magnetic flux and the floor in the heliospheric magnetic field. *Geophysical Research Letters*, *35*, 20108. https://doi.org/10.1029/2008GL035813
Papitashvili, V., Papitashvili, N., & King, J. (2000). Solar cycle effects in planetary geomagnetic activity: Analysis of 36-year long omni dataset. *Geophysical Research Letters*, *27*(17), 2797–2800. https://doi.org/10.1029/2000gl000064
Pizzo, V., Millward, G., Parsons, A., Biesecker, D., Hill, S., & Odstrcil, D. (2011). Wang-sheeley-arge-enlil cone model transitions to operations. *Space Weather*, *9*, 03004. https://doi.org/10.1029/2011SW000663
Pizzo, V. J., & Gosling, J. T. (1994). 3-d simulation of high-latitude interaction regions: Comparison with ulysses results. *Geophysical Research Letters*, *21*(18), 2063–2066. https://doi.org/10.1029/94gl01581
Riley, P. (2018). Statistics of extreme space weather events. In *Extreme events in geospace* (pp. 115–138). Elsevier. https://doi.org/10.1016/b978-0-12-812700-1.00005-4
Riley, P., Ben-Nun, M., Linker, J., Mikic, Z., Svalgaard, L., Harvey, J., et al. (2014). A multi-observatory inter-comparison of line-of-sight synoptic solar magnetograms. *Solar Physics*, *289*(3), 769–792. https://doi.org/10.1007/s11207-013-0353-1
Riley, P., Gosling, J. T., Weiss, L. A., & Pizzo, V. J. (1996). The tilts of corotating interaction regions at midheliographic latitudes. *Journal of Geophysical Research*, *101*(A11), 24349. https://doi.org/10.1029/96ja02447
Riley, P., Linker, J. A., Americo Gonzalez Esparza, J., Jian, L. K., Russell, C. T., & Luhmann, J. G. (2012). Interpreting some properties of CIRs and their associated shocks during the last two solar minima using global MHD simulations. *Journal of Atmospheric and Solar-Terrestrial Physics*, *83*, 11–21. https://doi.org/10.1016/j.jastp.2012.01.019
Riley, P., Linker, J. A., & Arge, C. N. (2015). On the role played by magnetic expansion factor in the prediction of solar wind speed. *Space Weather*, *13*(3), 154–169. https://doi.org/10.1002/2014sw001144
Riley, P., Linker, J. A., Lionello, R., & Mikic, Z. (2012). Corotating interaction regions during the recent solar minimum: The power and limitations of global MHD modeling. *Journal of Atmospheric and Solar-Terrestrial Physics*, *83*, 1–10. https://doi.org/10.1016/j.jastp.2011.12.013
Riley, P., Linker, J. A., & Mikić, Z. (2001). An empirically-driven global MHD model of the corona and inner heliosphere. *Journal of Geophysical Research*, *106*, 15889–15901. https://doi.org/10.1029/2000JA000121
Riley, P., Linker, J. A., Mikic, Z., Caplan, R. M., Downs, C., & Thumm, J.-L. (2019). Can an unobserved concentration of magnetic flux above the poles of the sun resolve the open flux problem? *The Astrophysical Journal*, *884*(1), 18. https://doi.org/10.3847/1538-4357/ab3a98
Riley, P., Lionello, R., Caplan, R. M., Downs, C., Linker, J. A., Badman, S. T., & Stevens, M. L. (2020). Using parker solar probe observations during the first four perihelia to constrain global magnetohydrodynamic models.
Riley, P., Lionello, R., Linker, J. A., Cliver, E., Balogh, A., Charbonneau, P., et al. (2015). Inferring the structure of the solar corona and inner heliosphere during the maunder minimum using global thermodynamic magnetohydrodynamic simulations. *The Astrophysical Journal*, *802*(2), 105. https://doi.org/10.1088/0004-637x/802/2/105
Riley, P., Lionello, R., Linker, J. A., Mikic, Z., Luhmann, J., & Wijaya, J. (2011). Global MHD modeling of the solar corona and inner heliosphere for the whole heliosphere interval. *Solar Physics*, *145*, 361–377. https://doi.org/10.1007/s11207-010-9698-x
Riley, P., Lionello, R., Linker, J. A., Mikic, Z., Luhmann, J., & Wijaya, J. (2012). Global MHD modeling of the solar corona and inner heliosphere for the whole heliosphere interval. *Solar Physics*, *274*, 361–377. https://doi.org/10.1007/s11207-010-9698-x
Riley, P., & Luhmann, J. G. (2012). Interplanetary signatures of unipolar streamers and the origin of the slow solar wind. *Solar Physics*, *277*, 355–373. https://doi.org/10.1007/s11207-011-9909-0
Riley, P., Mikić, Z., & Linker, J. A. (2003). Dynamical evolution of the inner heliosphere approaching solar activity maximum: Interpreting Ulysses observations using a global mhd model. *Annals of Geophysics*, *21*, 1347–1357. https://doi.org/10.5194/angeo-21-1347-2003
Riley, P., Mikic, Z., Lionello, R., Linker, J. A., Schwadron, N. A., & McComas, D. J. (2010). On the relationship between coronal heating, magnetic flux, and the density of the solar wind. *Journal of Geophysical Research*, *115*, 6104. https://doi.org/10.1029/2009JA015131

Scherrer, P., Amezcua, A., & Bogart, R. (2010). Access to solar dynamics observatory HMI and AIA data via the joint science operations center (JSOC). *AGU Fall Meeting Abstracts*, *2010*, SH23C–1867.

Scherrer, P. H., Bogart, R. S., Bush, R. I., Hoeksema, J. T., Kosovichev, A. G., Schou, J., et al. (1995). The solar oscillations investigation - Michelson Doppler imager. *Solar Physics*, *162*, 129–188. https://doi.org/10.1007/BF00733429

Scherrer, P. H., Schou, J., Bush, R., Kosovichev, A., Bogart, R., Hoeksema, J., et al. (2012). The helioseismic and magnetic imager (hmi) investigation for the solar dynamics observatory (sdo). *Solar Physics*, *275*(1–2), 207–227. https://doi.org/10.1007/s11207-011-9834-2

Schwadron, N. A., & McComas, D. J. (2008). The solar wind power from magnetic flux. *The Astrophysical Journal Letters*, *686*, L33–L36. https://doi.org/10.1086/592877

Solomon, S. C., Woods, T. N., Didkovsky, L. V., Emmert, J. T., & Qian, L. (2010). Anomalously low solar extreme-ultraviolet irradiance and thermospheric density during solar minimum. *Geophysical Research Letters*, *37*(16). https://doi.org/10.1029/2010gl044468

Svalgaard, L., & Cliver, E. W. (2007). A floor in the solar wind magnetic field. *The Astrophysical Journal Letters*, *661*, 203. https://doi.org/10.1086/518786